


Ka-band linearizer structure studies for a compact light sourceA. Castilla[Ⓜ],* R. Apsimon, and G. Burt[Ⓜ]†*Engineering Department, Lancaster University, Lancaster LA1 4YW, United Kingdom**Cockcroft Institute, Daresbury Laboratory, Warrington WA4 4AD, United Kingdom*X. Wu, A. Latina[Ⓜ], X. Liu[Ⓜ], I. Syratchev, and W. Wuensch[Ⓜ]*CERN, CH-1211 Geneva, Switzerland*B. Spataro[Ⓜ]*INFN-LNF, Via Enrico Fermi 40, 00044 Frascati, Rome, Italy*

A. W. Cross

Strathclyde University, Glasgow G4 0NG, United Kingdom (Received 29 April 2022; accepted 31 October 2022; published 9 November 2022)

The CompactLight design for a next-generation x-ray free-electron laser utilizes a C-band injector. This requires that the harmonic system used to linearize the beam's phase space must operate at X-band rf or higher. We investigate the optimum frequency for the harmonic system in the range of frequencies from 12 to 48 GHz. We describe the reasoning behind selecting 36 GHz (Ka-band) as our working harmonic frequency. The full linearizer system design including the power source, pulse compressor, and linearizing structure, along with options, is considered and presented. These designs are compared in terms of rf and beam dynamics performance. Two potential MW-level rf sources are discussed; a multibeam klystron and a gyro-klystron, while a klystron-based upconverter with an X-band driver is briefly discussed as an alternative path if even higher peak powers are needed. To further increase peak power, novel options for pulse compressors at Ka-band are discussed. Traveling and standing wave solutions for the structure are presented.

DOI: [10.1103/PhysRevAccelBeams.25.112001](https://doi.org/10.1103/PhysRevAccelBeams.25.112001)**I. INTRODUCTION**

The CompactLight design for a next-generation hard x-ray free-electron laser (FEL) facility utilizes state-of-the-art, high gradient, X-band (12 GHz) rf cavities. The facility will start with a C-band (6 GHz) injector—also denoted as Linac-0 in this paper—before transitioning to an X-band main linac, to take advantage of the higher gradients available at a higher frequency. In line with light source users' requirements, the facility will operate at a high repetition frequency, up to 1 kHz for the soft x-ray (SX) regime. Some of the operational parameters of the CompactLight electron linac are presented in Table I [1].

In order to generate short electron bunches—on the order of 1–5 fs—while maintaining a high bunch charge, XFELs

typically have longer bunch lengths in the injector, before bunch compression in a magnetic chicane. The compression is accomplished by imposing an energy chirp along the bunch before passing into the magnetic chicane so that the path length through the chicane is energy dependant, and through this, compressing the bunch in time. The energy chirp is induced by the injector rf system, operating off-crest from the peak of the voltage. However, as the voltage varies sinusoidally, this chirp is not linear in time. In order to linearize the chirp, a higher frequency rf cavity is used before the magnetic chicane, to correct the voltage distribution in time. The higher the frequency of this linearizing rf system, the lower the rf voltage that is required, with the voltage requirement roughly scaling proportional to the inverse square of the frequency [see Eq. (1)]. This would suggest that a higher frequency is ideal, nevertheless, there is a lack of high power, high frequency rf amplifiers, and the wakefields would be stronger with the smaller apertures required for these higher frequencies. In this paper, we investigate the design of a Ka-band (36 GHz) rf system, as a working point, suitable to use as a linearizer.

Ka-band rf systems are not new in particle accelerators, as the original frequency for the compact linear collider

*Also at CERN

†g.burt@lancs.ac.uk

TABLE I. Electron beam parameters for the CompactLight source.

Parameter	Value			Units
Nominal bunch charge	75			pC
Peak current at injector	20			A
Normalized emittance	0.15			$\mu\text{m rad}$
Photon energy range	SX	SX	HX	...
Shortest FEL wavelength	2.5	0.6	0.08	nm
Repetition rate	1	0.1	0.1	kHz
Final beam energy	1	2–2.4	5.5	GeV
Final peak current	0.35	≤ 5	≤ 5	kA
Final bunch length, rms	~ 220	~ 17	~ 17	fs

(CLIC) was 30 GHz [2], an extensive high-power and high-gradient testing was carried out in CTF2 [3] and CTF3 [4]. For CLIC, a Ka-band amplifier was not required due to the novel two-beam acceleration scheme, where a high current secondary beam is decelerated in a power extraction and transfer structure (PETS) to generate the required rf power [5,6]. However, Ka-band gyro-klystron amplifiers up to 15 MW have been produced by Gycom [7], but those were unable to operate at the high repetition frequencies required for CompactLight (up to 1 kHz). Here we consider the design of two rf amplifiers, a gyro-klystron and a higher-order mode, multibeam klystron (HOMMBK). These sources themselves do not produce sufficient power to drive the rf structure to the required gradients, hence, a pulse compressor system is also considered. Both traveling wave and standing wave structures are developed in this paper.

First, in Sec. II of this paper, we describe the FEL beam dynamics' requirements for the linearizing system, in terms of the structure's aperture due to the effects of the transverse wakefields (Sec. II A), as well as the integrated voltage needed for the bunch linearization (Sec. II B). Then, in Sec. III, we compare the performance of different frequencies for the harmonic system and choose 36 GHz as the working point. We also present two different structure alternatives: a constant impedance traveling wave structure (TWS) and a standing wave structure (SWS), we briefly mention, but not discuss in detail, a small aperture, high gradient standing wave (SW) option, all of them described in Secs. IV–VI, respectively. Section VI also lays out how the use of a copper SWS, at cryogenic temperatures (77 K), could reach higher gradients, if a more compact structure is required. Finally, in Sec. VII, we summarize our findings and outline the proposed baseline system for the CompactLight's linearizing system.

II. REQUIREMENTS FOR A LINEARIZER

In CompactLight, the bunch length at the linearizer is about 300 μm , long enough for the bunch to feel the rf curvature of the X-band accelerating structures preceding the linearizer. This curvature must be removed in order to achieve the required compression factor after the magnetic

compressing chicane. To effectively linearize the bunch, the linearizer structure should operate at a phase of about 180° , i.e., in decelerating mode. From this, it is easy to understand that the higher the voltage needed to linearize the bunch, the greater the accelerating voltage would be needed from the main Linac to compensate for this deceleration. With this assumption, the required integrated voltage (V_{lin}) can be estimated using a simple analytic expression:

$$V_{\text{lin}} = \frac{1}{h^2} V_C \cos(\phi_C), \quad (1)$$

where V_C is the integrated voltage of the C-band structures in Linac-0 [1], and ϕ_C is the operating phase of the Linac-0 structures. If we consider, for example, a harmonic number of $h = 6$, with respect to the C-band injector (i.e., a 36-GHz linearizer), the fraction in Eq. (1) becomes a factor of $\frac{1}{36}$ and $V_{\text{lin}} \equiv V_{\text{Ka}}$. A first estimate, considering that the Linac-0 operates at a 20 MV/m accelerating gradient with a phase of about 25° (to accelerate the bunch—up to 300 MeV—while imparting the required energy chirp), gives $V_{\text{Ka}} \approx 8.3$ MV. In practice, the actual integrated voltage is different from this number—typically lower—because the correlated energy spread introduced by the longitudinal wakefield contributes to the linearization.

Besides affecting the economy of the longitudinal phase-space manipulations along the facility, the short-range wakefield also introduces unwanted transverse head-to-tail deflections in the bunch that can lead to emittance dilution and, if too strong, single-bunch beam-breakup. Considering that the bunch at the location of the linearizer is relatively long and its average momentum is just 300 MeV, the effect of the short-range wakefield defines the minimum iris aperture radius (a) of the linearizer, which has been fixed at 2 mm, the arguments that describe quantitatively the reasoning behind this value are described in the subsections below.

A. Action amplification factor

The effect of the transverse wakefield is that the bunch head, while traversing a structure with an offset due for example to a regular betatron oscillation, excites a kick that pushes the bunch tail to a new betatron oscillation of larger amplitude. The increase in the betatron amplitude induces growth of the projected emittance and can even lead to bunch breakup. One can define an amplitude amplification factor, or “action amplification factor,” $A(z)$, to evaluate the action increase as a function of the distance from the head of the bunch, z ,

$$A(z) = \frac{J_f}{J_i} \approx 1 + \frac{1}{2} \left(\beta \frac{e Q w_{\perp}(z) L_{\text{Ka band}}}{E_{\text{beam}}} \right)^2. \quad (2)$$

In the formula, J_i and J_f indicate, respectively, the action before and after the linearizer structure, β is the optical beta

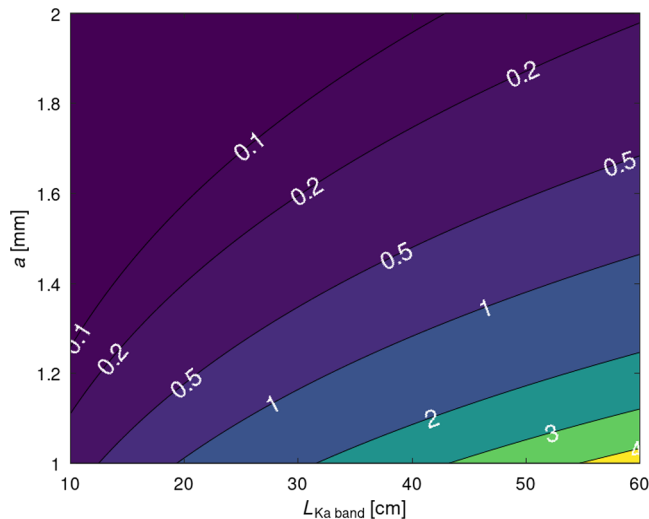


FIG. 1. The fraction of the action amplification factor exceeding 1 under the effects of short-range wakefields in the Ka-band linearizer, as a function of the Ka-band length and of the iris aperture radius.

function at the structure, e is the electron charge, Q is the total bunch charge, $L_{\text{Ka band}}$ is the rf active length of the Ka-band linearizer, E_{beam} is the beam energy, and $w_{\perp}(z)$ is the wake potential expressed in V/pC/m/mm following the approximation defined in [8].

Due to wakefields, the allowed aperture size is limited by a minimum radius a , which is dependent on the cavity length, as given in Fig. 1. We define as “acceptable” fractions of the action amplification factor below 0.1, i.e., <10% amplification. Based on these criteria, the selected working point, for a Ka-band linearizer, corresponds to $L_{\text{Ka band}} = 30$ cm and $a = 2$ mm.

B. Integrated voltage of the Ka-band

The effectiveness of the Ka-band linearizer can only be measured by looking at the bunch shape at the linac end and, ultimately, at the photons generated in the undulator. In order to be effective, the effect of the Ka-band linearizer must be combined with the effects of all components of the whole CompactLight facility. Effects such as the longitudinal wakefields and the rf curvature of the three linacs: the C-band Linac-0, plus the X-band Linac-1 and 2, as well as the Ka-band itself, including also the nonlinearities introduced by the magnetic chicanes of the two bunch compressors, BC1 and BC2, located between Linac-0 and Linac-1, and Linac-1 and Linac-2, respectively. All these contribute to alter the bunch’s longitudinal phase space and the intensity profile of the bunch.

Given such numerous nonlinear effects, occurring in the longitudinal plane along the tracking, only a start-to-end optimization including all the relevant effects can provide the optimized integrated voltage. We used the 1D tracking code “Track1D” to perform the longitudinal optimization of

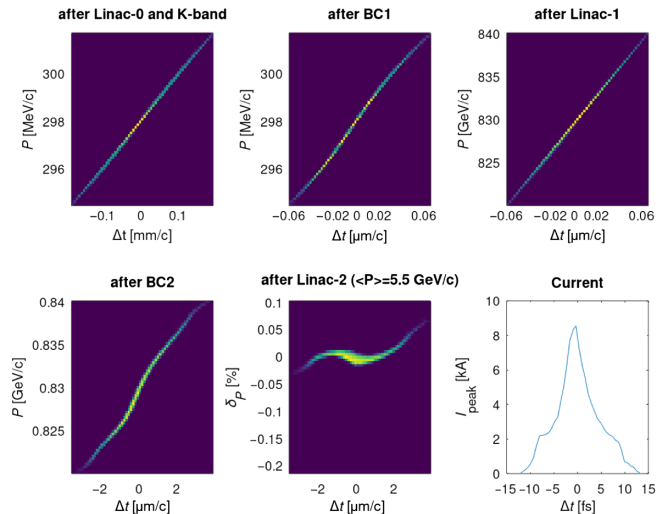


FIG. 2. Example of start-to-end tracking in CompactLight, obtained with the code Track1D.

the phase space. Figure 2 shows an example of start-to-end tracking in CompactLight, obtained with the code Track1D [9].

The resulting required maximum integrated voltage—for a Ka-band linearizer—was then fixed at $V_{\text{Ka}} = 12.75$ MV, including a safety factor.

III. FREQUENCY OPTIONS

After performing an iterative analysis between the TWS electromagnetic design and the beam dynamics calculations, an absolute minimum iris radius (denoted as a) was fixed at 2 mm—to be able to digest the adverse wakefield contributions from the linearizer—as detailed in the previous section of this paper. This is already a relatively large aperture for the cavity size at these frequencies ($a \approx R/2$ for the Ka-band, see Fig. 3), which means that a bigger iris aperture would further compromise the cavity shunt impedance while going to smaller apertures would have a negative impact on the wakefield contributions to the beam dynamics. Therefore, an executive decision was taken to opt for a constant impedance structure, simplifying the manufacturing process to a single type of disk (excluding the matching cells at the input and output ports). Figure 3 shows the geometrical parameters of the single cell design.

After some iterations of the CompactLight project layout, it was decided to go for a 6-GHz injector. Once the baseline was set to have a full C-band injector, it opened up several possibilities for the selection of the harmonic linearizer system (i.e., $h = 2, 3$, etc.). To aid the choice of frequency for such harmonic system, Fig. 4 presents a comparison between parameters of the optimized single cells—with a 2-mm iris aperture—for several suitable frequencies. From these plots, we can see that higher frequency options have both higher shunt impedances

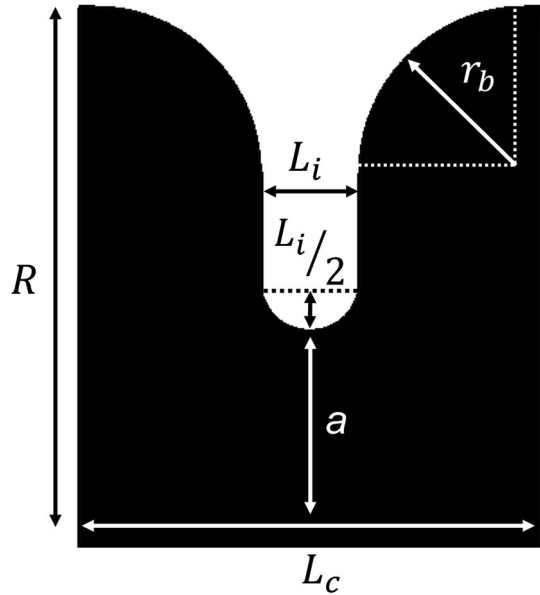


FIG. 3. Geometrical parameters of the single cell.

and Q factors (top), while maintaining higher group velocities, and therefore, lower attenuation factors (bottom).

As further means of comparison, we now consider the specific case of the 36-GHz—constant impedance—TWS,

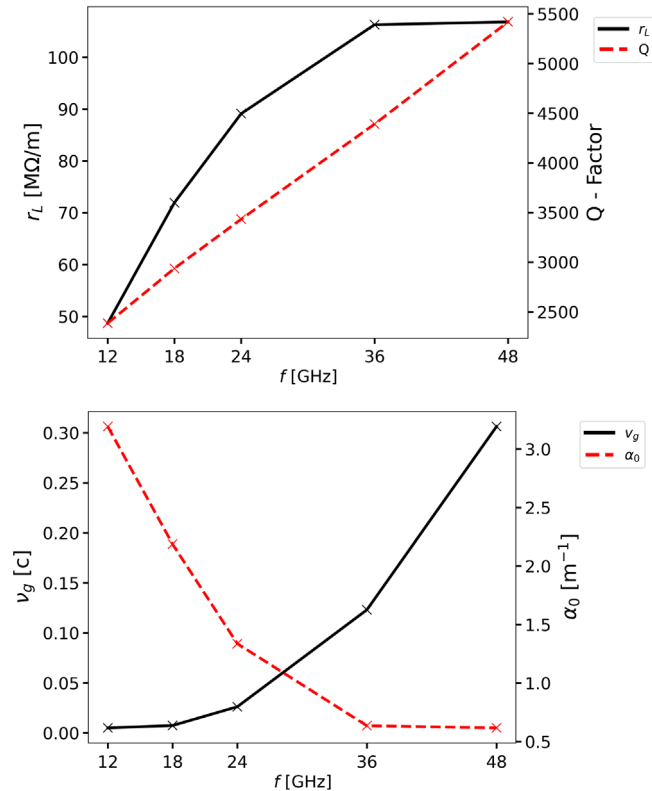


FIG. 4. Parameter comparison of a $2\pi/3$ single cell at different frequencies for a 2-mm iris radius.

with a 2-mm iris aperture, and look at the single cell parameters as a function of phase advance (ϕ), see Fig. 5.

From Fig. 5, we can see that both higher shunt impedances and quality factors favor higher phase advances (top), while higher group velocities favor lower phase advances (bottom) and that the attenuation factor (α_0) has a minimum at $\phi = 2\pi/3$. A particular behavior of structures with these large apertures can be seen in Fig. 5 for $\phi < 120^\circ$, which makes the cell lengths shorter (i.e., smaller phase advance) and significantly increases the attenuation. In order to evaluate the optimum frequency and phase advance, it is necessary to compare the required power to reach the design gradient and the required mechanical tolerances. Starting with the latter, we have derived some useful relations to assess the change in phase advance with dimensional tolerances for different designs. The frequency of a given phase advance for a disk-loaded structure is given by

$$\omega = \omega_{\pi/2} + \kappa \cos(\phi), \quad (3)$$

where κ is the cell-to-cell coupling and ϕ is the phase advance. Hence the group velocity is given by

$$v_g = \frac{d\omega}{dk} = -\kappa L_c \sin(\phi), \quad (4)$$

where L_c is the length of each cell, and hence by differentiating the frequency with respect to the phase advance and

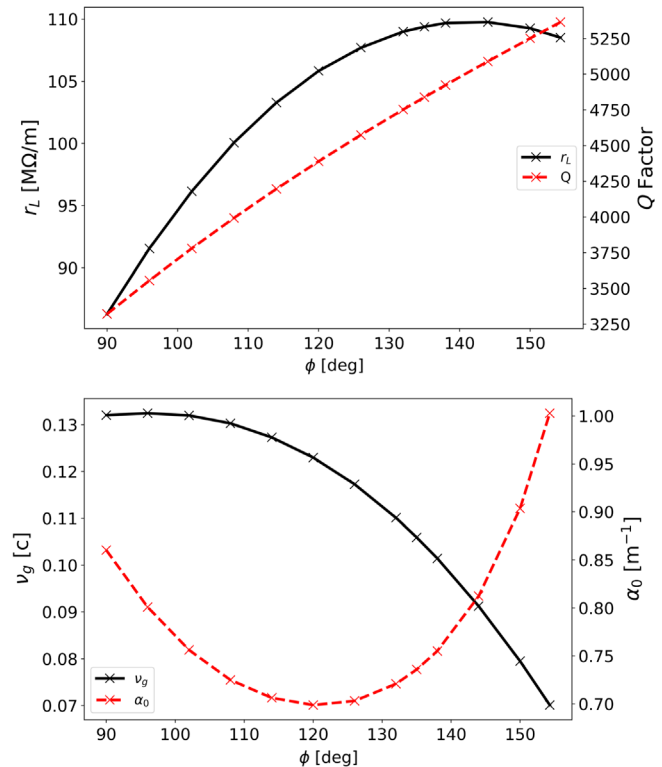


FIG. 5. Parameter comparison of a 36-GHz single cell with a 2-mm iris radius for different phase advances.

rearranging, we find that the change in phase advance with frequency, per cell, is

$$\left. \frac{d\phi}{d\omega} \right|_{\text{cell}} = \frac{L_c}{v_g} = \frac{c\phi}{\omega v_g}. \quad (5)$$

For a pillbox cavity, the resonant frequency is given as

$$\omega = \frac{\xi c}{x}, \quad (6)$$

where ξ is the root of the first Bessel function, and x is the cavity radius. Therefore, the change in frequency with a change in radius is

$$\frac{d\omega}{dx} = -\frac{\xi c}{x^2} = -\frac{\omega^2}{\xi c}. \quad (7)$$

Combining Eqs. (5) and (7), we reach

$$\left. \frac{d\phi}{dx} \right|_{\text{cell}} = \left. \frac{d\omega}{dx} \frac{d\phi}{d\omega} \right|_{\text{cell}} = -\frac{\omega}{\xi} \frac{\phi}{v_g}. \quad (8)$$

As one would expect, the tolerances relax as the group velocity increases or the frequency decreases, hence we can maintain the same tolerances as we increase the cavity's frequency by also increasing the group velocity. The dependence on the phase advance is due to the cell length increasing proportionally to the phase advance to maintain synchronism with the beam. However, it should be noted that if the phase advance changes, the phase with respect to the beam increases with each sequential cell. Yet, as the cell length increases with phase advance and decreases with frequency, the allowed deviation from the design phase advance also increases proportionally to the phase advance. One might expect the allowed phase advance deviation to also be frequency dependant, nevertheless in the case of a linearizer cavity, the required voltage, and hence cavity length, decreases with frequency, so this dependence should not be the main driver of the tolerance limitations. To obtain the total change of the phase advance by a given manufacturing error in the entire structure, we should multiply Eq. (8) by the total number of cells. Where

$$N_{\text{cells}} = \frac{L_{\text{Total}}}{L_c} = \frac{\omega L_{\text{Total}}}{c\phi}, \quad (9)$$

and finally, we obtain

$$\frac{d\phi}{dx} = \left| \frac{d\phi}{dx} \right|_{\text{cell}} N_{\text{cells}} = \frac{\omega^2 L_{\text{Total}}}{c v_g \xi}. \quad (10)$$

To do a quick comparison, Fig. 6 shows the accumulated phase advance change, for a structure of $L_{\text{Total}} = 30$ cm

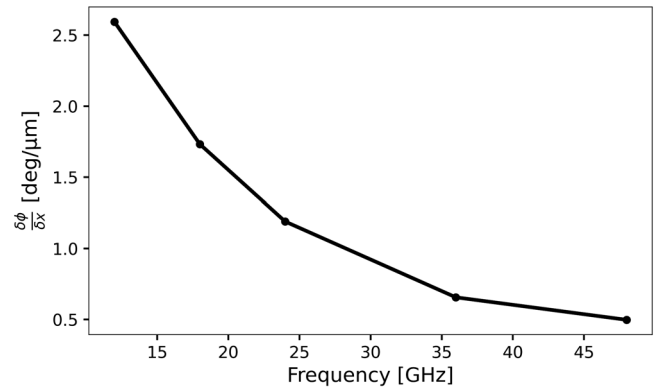


FIG. 6. Accumulated phase advance error given by manufacturing tolerances for a 30-cm structure and 2-mm iris aperture radius at different frequencies.

and 2-mm iris aperture radius, as a function of frequency, for a given cell-to-cell phase advance error.

Another important thing to keep in mind while comparing the frequency options is that the voltage needed from the linearizer scales, at first order, as $1/h^2$ [see Eq. (1)], where h is the harmonic number with respect to the injector's frequency, hence, below certain frequency, one gets gradient limited (i.e., longer structures are needed). Also, as discussed before, lower linearizer voltages would require less compensation from the main Linacs (Linac-1 and 2), facilitating the compactness of the machine's total length. This dictates that higher frequencies are preferable for this application. Shorter structures are needed for higher frequencies, however, above certain frequency, one gets power limited. After taking into consideration all the aforementioned aspects—both quantitative and qualitative—and capitalizing on the experience that CLIC has with Ka-band systems, we reached the decision that 36 GHz ($h = 6$) was a good compromise for the linearizer system, joining both high performance and lower harmonic voltage needed.

Taking a closer look into the 36-GHz option, we can plot the accumulated phase advance change—for a 30-cm structure with $a = 2$ mm—as a function of the cell-to-cell phase advance (ϕ).

Figure 7 shows that lower phase advances result in a lower total change of the phase advance, for a $L_{\text{total}} = 30$ cm, $a = 2$ mm, Ka-band structure. Yet, $\phi = 120^\circ$ is deemed as a good compromise to keep relaxed tolerances and high shunt impedance (see also Fig. 5) simultaneously.

Finally, we can take a closer look at the power requirement for a Ka-band, 30-cm long linearizer, for different phase advances (see Fig. 8).

From Fig. 8, we can appreciate that the input power required to produce 12.75 MV of integrated voltage in the TWS drops with the phase advance, first gradually, and after 120° , it does so more sharply. Hence, from the power consumption viewpoint, higher phase advances are desirable.

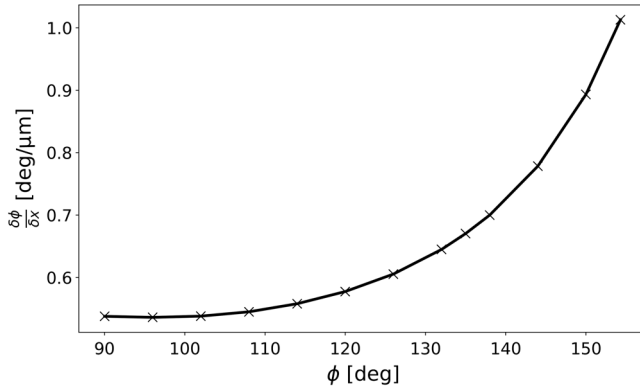


FIG. 7. Accumulated phase advance error given by manufacturing tolerances for a 30-cm Ka-band structure with a 2-mm iris aperture radius as a function of the designed cell-to-cell phase advance.

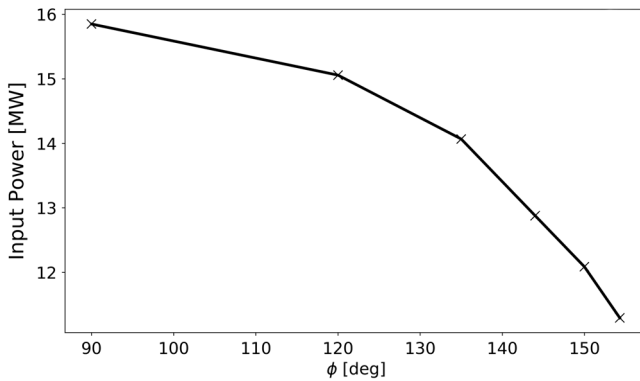


FIG. 8. Power requirement for a 30-cm, 36-GHz structure, to provide 12.75-MV integrated voltage, for different phase advances.

Since the tolerance analysis, made earlier in this section, favors lower phase advances, we conclude again that $\phi = 2\pi/3$ is a reasonable compromise for our system.

For the rf power source for the Ka-band linearizer, we consider two main options published recently elsewhere: a gyro-klystron which uses a rotating beam to interact with a single mode [10,11] and a HOM multibeam klystron that uses multiple beams so that other modes are canceled out [12]. The gyro-klystron and multibeam klystron can provide 3.2 and 2.5 MW, respectively. This power level is smaller than the required input power for the linearizer hence a pulse compression scheme must be used to increase the peak rf power to reach the required voltage.

The Q factor of a SLEDI cavity needs to be around 10^5 . However, the Q factor of a resonant cavity at 36 GHz could not reach that value. Therefore, a delay line-based, dual-mode SLEDII pulse compressor is more suitable for the CompactLight linearizer system [13–18].

The dual-mode delay line needs to have an approximate length of 1.43 m to produce a 20-ns pulse, which includes

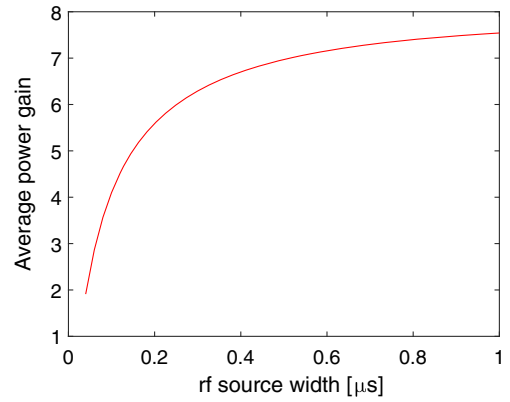


FIG. 9. Power factor gained by a 20 ns pulse coming out of the pulse compressor, as a function of rf power source pulse width.

the filling time and rise/fall edge of the rf power source. Figure 9 shows the average power gain for the dual-mode SLEDII as a function of the pulse width coming from the rf source, from this, we can see that an average power gain of 6.97 is reached when the rf power source width is 510 ns. This means that the average peak power of the compressed (20 ns) pulse, fed to the linearizer, could reach up to 15 MW, using either of the above-mentioned rf sources (i.e., a gyro-klystron [10] or a HOM multibeam klystron [12]).

IV. KA-BAND TRAVELING WAVE STRUCTURE

A. Reentrant option

Before continuing the discussion laid out in Sec. III of this paper, it is worth mentioning that a full study of the parameter space was performed for the single cell, including a comparison between a reentrant and a simple cell option. To illustrate this, Fig. 10 shows the geometric parameters of the nose cones, while Fig. 11 presents a scan of the nose cone length (NCL) for the optimal values of the nose cone height (NCH = 0.1 mm) and the nose cone

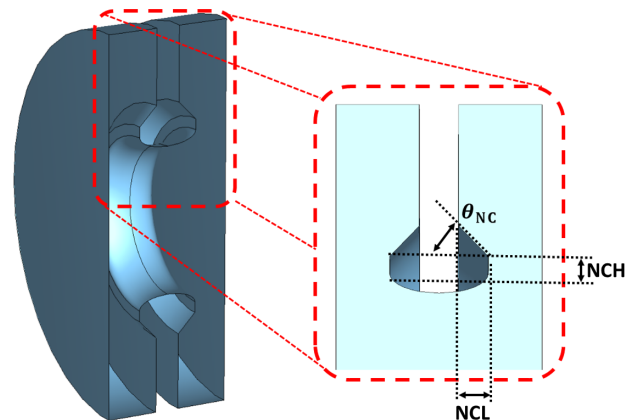


FIG. 10. Geometric parameters of the nose cone for a reentrant cell option.

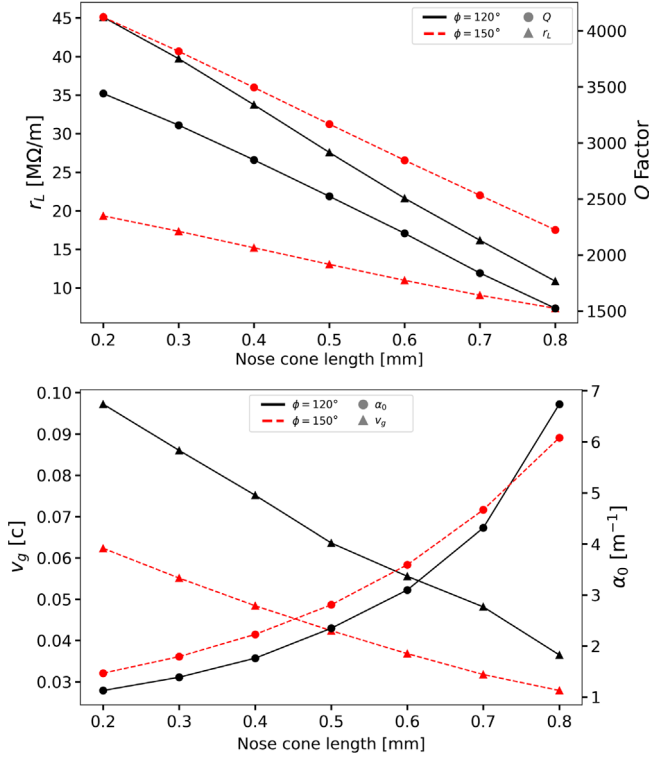


FIG. 11. Example of the nose cone’s optimization process for a reentrant cell option. In this case, $NCH = 0.1$ mm and $\theta_{NC} = 45^\circ$.

angle ($\theta_{NC}=45^\circ$). Please note that these values correspond to a cell without cavity blending radius (i.e., $r_b = 0$), while the optimized disk-loaded cell described in Sec. IV B has a blending radius of $r_b = 1$ mm.

Figure 12 shows the integrated voltage reached by a 30-cm reentrant structure and 15 MW of input power and is presented to contrast against Fig. 8, where, for example, a $2\pi/3$ -simple structure would reach 12.75-MV integrated voltage for the same input power and the same length. Granted this is not a one-to-one comparison, since $r_b = 0$ for the reentrant cell, versus $r_b = 1$ mm for the disk-loaded

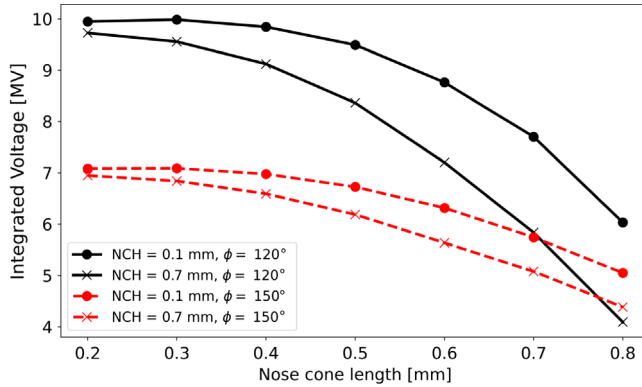


FIG. 12. Integrated voltage for a 30-cm long reentrant structure and 15 MW of input power.

simple cell. Nevertheless, one can expect the integrated voltage of the reentrant design to converge to the same value obtained for the disk-loaded simple cell when the nose cone length goes to zero, but it will decrease with the nose cone length, as illustrated in Fig. 12, showing by comparison that, for our case of study, the optimal voltage output for a given power input for the reentrant design is, at best, equal to that of a disk-loaded design. We keep in mind that a re-entrant design would also incur extra manufacturing complications due to the nose cones, rendering the disk-loaded simple cell better suited for our application. For brevity, we will skip over the standard optimization process of the simple disk-loaded cell, to directly state its optimized parameters for different phase advances.

B. Disk-loaded simple cell option

The TWS single cell geometry was optimized for different phase advances at 36 GHz, and the general parameters of each one are presented in Fig. 5. Table II presents the parameters for three of these options (i.e., $\phi = 90^\circ$, 120° , and 154.3°) for a quick numerical comparison. Perhaps the parameter decision that is least compelling corresponds to the iris thickness (L_i), since the chosen value of 0.6 mm was not optimal in the general sense. However, from the standpoint of phase stability, the thinner the iris, the less sensitive the cell is to manufacturing errors (see Fig. 13). In our design, we are assuming manufacturing tolerances of 5 μm [19]. Hence, following Fig. 13, an iris thickness of 0.6 mm was chosen as a compromise, i.e., $d\phi < 3^\circ$, which is consistent with what is accepted for X-band structures [20]. If the manufacturing errors are improved, or the phase requirements relaxed, one may consider thicker irises (e.g., ≈ 1 mm for this geometry) for improved rf performance.

From Table II, we observe that for a structure with relatively large apertures—like this one, where $a \approx \lambda/4$ —going from phase advances of $\pi/2$ to $5\pi/6$, the Q factor and shunt impedance are increased by $\sim 63\%$ and $\sim 21\%$,

TABLE II. TWS single cell parameters.

Parameter	$\phi = \pi/2$,	$2\pi/3$,	$5\pi/6$	Units
Frequency f		36		GHz
Q factor	3322	4390	5251	...
Shunt impedance r_L	86	106	109	MΩ/m
Group velocity v_g	0.132	0.123	0.080	c
Attenuation α_0	0.85	0.70	0.90	m ⁻¹
Peak surface field E_p^a	2.29	2.57	2.99	MV/m
Peak surface field B_p^a	4.41	4.45	4.76	mT
Cavity radius R	4.05	3.95	3.86	mm
Iris radius a		2.00		mm
Cell length L_c	2.08	2.78	3.47	mm
Iris thickness L_i		0.60		mm
Cavity blending radius r_b		1.00		mm

^aNormalized to $E_{acc} = 1$ MV/m

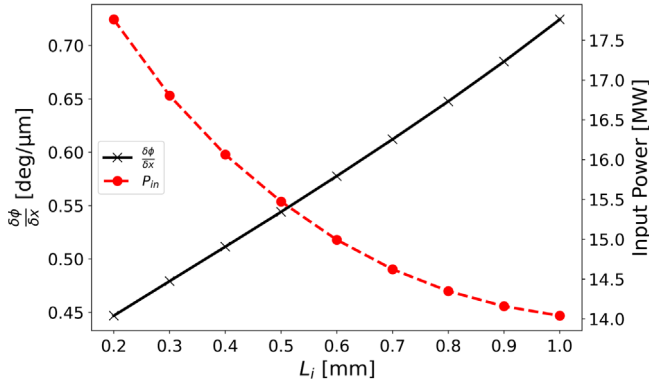


FIG. 13. Accumulated phase advance error and power needed to reach 12.75 MV of integrated voltage for a $2\pi/3$, 30-cm structure, as a function of the iris thickness for the disk-loaded simple cell.

respectively. While the group velocity is reduced by 5% of the speed of light, we only see a $\sim 6\%$ increase in the attenuation factor. The peak surface magnetic field increases only by $\sim 8\%$, while the peak surface electric field only increases by $\sim 30\%$. Finally, and as expected, the length per cell increases by up to 67%, between $\phi = \pi/2$ and $5\pi/6$. As mentioned before, from the power requirements viewpoint, higher phase advances are preferred, while, for maintaining reasonable manufacturing tolerances and more balanced surface fields, lower phases are more favorable. Therefore, we are reaffirming the choice of a $2\pi/3$, 300-mm long (108 cells), constant impedance TWS, as the linearizer baseline for the CompactLight application, which is capable of reaching the required 12.75 MV of integrated voltage, for a feasible input power of 15 MW after compression.

Table III shows the operational parameters of the baseline structure at the required integrated voltage for the bunch linearization.

A practical tolerable limit on the higher gradient operation came out recently from the experimental activity [21–23] by estimating the modified Poynting vector (S_c) and pulse heating effects. The breakdown rate is a measure of the rf sparks per unit time and length inside an accelerating

TABLE III. TWS parameters at nominal voltage.

Parameter	Value	Units
Active length l	300	mm
Phase advance ϕ	$2\pi/3$	rad
Number of cells	108	...
Filling time τ	8.4	ns
Frequency f	36	GHz
Compressed power P	15	MW
Design gradient E_{acc}	42.5	MV/m
Peak surface field E_p	109.2	MV/m
Peak surface field B_p	189.1	mT
Modified Poynting vector S_c	4.84	W/ μm^2

TABLE IV. Comparison of average dissipated power.

Structure	Repetition rate [Hz]	Average dissipated power [kW/m]
CLIC	50	3.06
CompactLight main linac	1000	2.44
Ka-band 300 mm TWS	1000	2.47

structure. For the structure proposed in this section, the peak fields: $E_p \approx 109$ MV/m, $B_p \approx 189$ mT, and $S_c \approx 4.8$ W/ μm^2 , at a nominal gradient, are all within the practical limits of operation for a sub-20 ns pulse. Also, a 108-cell structure is deemed feasible from the manufacturing viewpoint, and a filling time of 8.4 ns allows for a good performance of the pulse compressor (see Fig. 9).

Table IV shows a comparison of the power dissipation between the Ka-band linearizer and two X-band TWS examples. The power dissipation of the Ka-band (2.5 kW/m) linearizer is comparable to that of the CompactLight main linac (2.4 kW/m), when both are operating at a 1-kHz repetition rate. This makes the Ka-band TWS a consistent option for this application, in terms of its power dissipation. One may feel inclined to think that the important difference in surface area between the Ka-band and the X-band structures would play the main role in the capability of dissipating these power levels, and hence, expect that the Ka-band would be susceptible to thermal runaway. However, we will soon describe how the relatively short and wide thermal paths, given by the cell irises, are the valid reasons why this is not the case [see Eq. (11)].

Finally, a preliminary thermal analysis has been done on the single cell geometry to address the thermal losses. Typically, normal conducting rf cavities have their temperature regulated via cooled, turbulent water flowing at high mass flow rates through metal pipes joined to the cavity. For a sufficiently high mass flow rate, the pipes and the cavity surfaces in contact with them can be held at a fixed temperature. However, there will always be a temperature gradient between the rf surface—where the heat is applied in the skin depth—and the cavity surfaces in contact with the pipes. This thermal gradient is maximum across the iris, so a simple model of the linear heat flow through an iris is considered here. For an iris approximated as a cylinder of internal diameter d , and thickness between the iris aperture and the cooling pipe t , with thermal losses on the iris, \dot{Q} , applied to the inner diameter, and the outer surface held at a fixed temperature, the temperature difference between the inner and outer surfaces, ΔT , is given by

$$\Delta T = \frac{\partial \dot{Q}}{\partial z} \frac{\ln(1 + 2t/d)}{2\pi\kappa}, \quad (11)$$

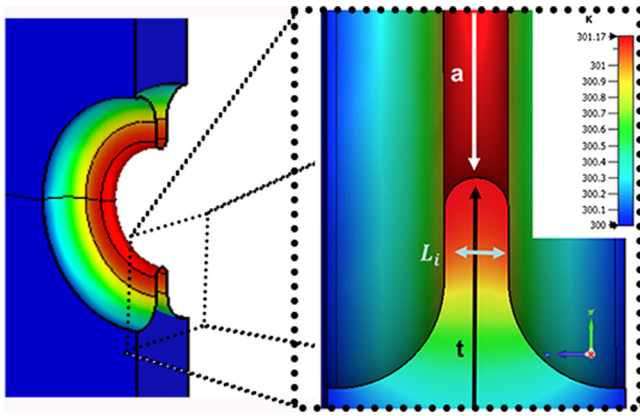


FIG. 14. Cross section of a single cell and CST® steady-state thermal simulations results at peak gradient.

where κ is the thermal conductivity of the cylinder. We find that for a given temperature rise, if we scale a structure linearly in frequency, where t/d remains constant, then, the maximum power loss per unit length is also constant. It is important to mention that in our analytical model, we assume that only half of the power is deposited in the iris, while the power deposited in the equator does not contribute to the temperature rise, since it is dissipated in the thick section of the body, close to the cooling water channels. Following this logic, we conclude that although the Ka-band structures are significantly smaller than the X-band structures, they should be capable of handling the same 2.44 kW/m as the main linac.

This linear heat transfer analysis was followed by thermal simulations in the CST® studio suite. Since the iris is the highest temperature point, and by the fact that this design has a large aperture, an interesting outcome of the simulations is that the thermal path between the tip of the iris and the cavity body remains relatively short and wide, making the heat transfer to the copper volume, and eventually the cooling channels, easy and quick. Therefore, using cooling channels of 10 mm diameter and water at 27° C, at the peak gradient of 42.5 MV/m, we observe an increment of only 1° on the iris in the steady state for an average power loss of 2.47 kW/m (see Fig. 14). This temperature rise is only due to the conduction of the iris and it does not take into account temperature rises in the water itself, or the water boundary layer. However, these can always be addressed by lowering the temperature of the water, if deemed necessary. For all these reasons, we consider that the cooling should not pose a considerable challenge to the operation of this structure.

C. Couplers

In order to feed the 30-cm TWS with a TM₀₁ mode, a double feed mode launcher was designed as a coupler. Figure 15 (top) shows the mode launcher's topology, composed of two rectangular waveguides (WG)—symmetrically placed in the vertical direction—feeding a horizontal

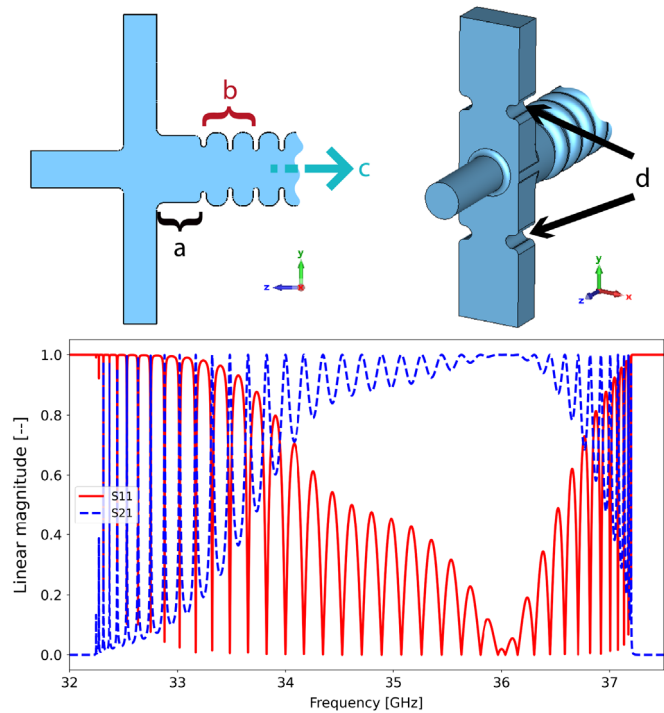


FIG. 15. Mode launcher geometry (top) and S-parameters for a 10-cm long structure (bottom).

cylindrical waveguide (labeled as “a”), two matching cells (M cells), labeled as “b”, follow the cylindrical waveguide and are directly connected to the rest of the structure (“c”). Figure 15 (bottom) also shows the S-parameters for a 10-cm long structure, as an illustration of its performance. It can be appreciated, in Fig. 15 (top), the inclusion of inductive notches in the mode launcher's rectangular waveguides (labeled as “d”). These notches, along with a matching cell after the mode launcher's circular waveguide, are used to tune the coupling and eliminate any residual standing wave due to internal reflections in the structure.

Table V enlists the main geometrical parameter associated with the mode launcher design.

In order to minimize rf losses in transportation, the waveguides will operate in the TE₀₁ mode of a circular waveguide. This mode easily converts into the TE₂₀ mode of a rectangular waveguide. A mode converter option was

TABLE V. Mode launcher geometrical parameters.

Parameter	M-cell 1	M-cell 2	Units
Cylindrical-WG radius	3.32		mm
Cylindrical-WG length	4.58		mm
Cavity radius R	3.94	3.95	mm
Iris radius a (left/right)	2.41/2.3	2.3/2.0	mm
Cell length L_c	2.85	2.78	mm
Iris thickness L_i		0.60	mm
Cavity blending radius r_b		1.00	mm

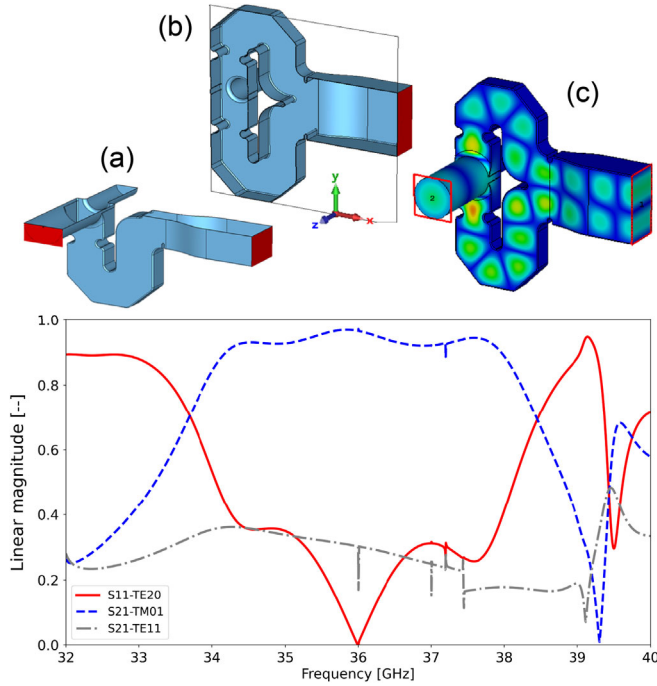


FIG. 16. TE20 to TM01 mode converter's horizontal (a) and vertical (b) cross sections, field pattern distribution (c), and its matched S-parameters (bottom).

designed in an effort to simplify a low loss transport network. Such a converter couples to a TE20 mode—coming directly from a low loss rectangular waveguide—and feeds symmetrically a TM01 circular mode to the structure's mode launcher (see Fig. 16).

This mode converter requires the feeding paths to the mode launcher to be asymmetrical, which allows for the correct power flow into the structure. Inductive notches are introduced at the side of the splitting bifurcation to control and reduce any standing wave trapped in this section. There is, however, a residual standing wave that stays present in such TE20 to TM01 mode launcher. Nevertheless, we believe that it has been reduced to a practical level and it can be further optimized if deemed necessary. Figure 16 (bottom) shows the linear magnitude of the mode converter's S_{11} parameter (solid red line), this parameter represents the reflection of the TE20 mode at the input port. Figure 16 also shows the transmission of the TM01 mode going to the structure, described by the S_{21} -TM01 parameter (dashed blue line). The TE20-to-TM01 transmission, at 36 GHz, is sufficiently broadband for this application and even when it is clearly not 100% efficient, since there is a small transmission of a spurious TE11 mode, indicated by the S_{21} -TE11 parameter (dash-dotted gray line), still makes this design a suitable coupler for the TWS. The width (hx) of the inductive notches can be used to reduce the minimum reflection (see Figs. 16 and 17), and the blend radius of the immediate WG corner (rx)—with respect to the WG bifurcation—is used to maintain this minimum at the

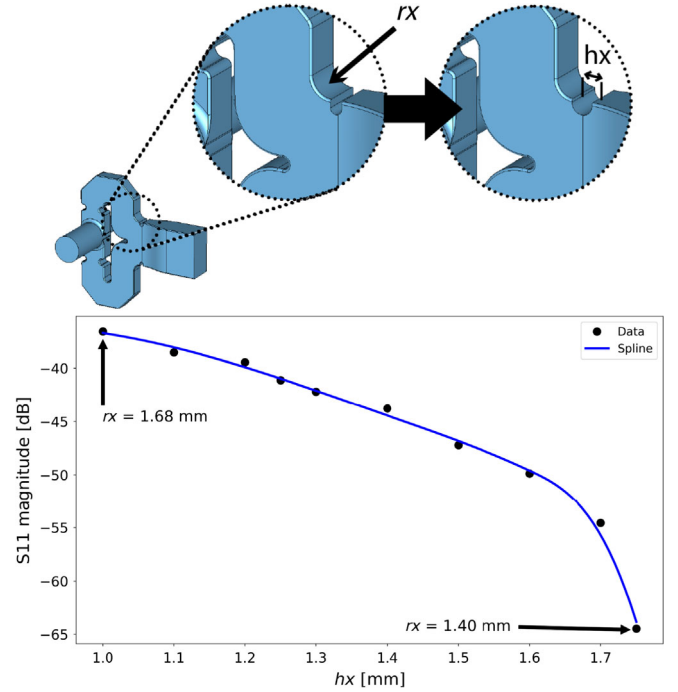


FIG. 17. Geometrical parameters rx and hx (top). The magnitude of the mode converter's minimum reflection, tuned to 36 GHz, as a function of hx (bottom).

desired frequency of 36 GHz. This ensures the right mode propagation into the structure, at the desired frequency. Figure 17 shows the related geometrical parameters hx and rx (top), and the magnitude (in dB) of the S11-parameter minimum, always tuned to 36 GHz (bottom).

From Fig. 17 (bottom)—disregarding the change in rx to tune the minimum reflection to 36 GHz—we can see the dependency between the reflection's level and the notches width hx . Hence, we find for our design a value of $hx = 1.75$ mm and $rx = 1.4$ mm.

D. Wakefields

In order to benchmark the wakefields effects discussed in Sec. II of the present paper, we have performed longitudinal and transverse wakefield simulations for a 30-cm long structure with couplers, but not the mode converter, to take advantage of the symmetry planes in the—already heavy—simulation of the full structure [see Fig. 18 (top)]. Figure 18 (bottom) shows the magnitude of the longitudinal (dash-dotted blue line) and transverse (dashed red line) short-range wakefields for a single, 75 nC, 300 μ m electron bunch (solid black line).

Up to this point, we are only considering the short-range wakefields, since the machine operates in a single bunch scheme. However, a two-bunch operation has also been proposed for CompactLight, where the spacing between bunches is in the order of 500 ps (~ 150 mm). Figure 19 shows the long-range wakefields excited by the first bunch, as seen by a second bunch arriving 500 ps later.

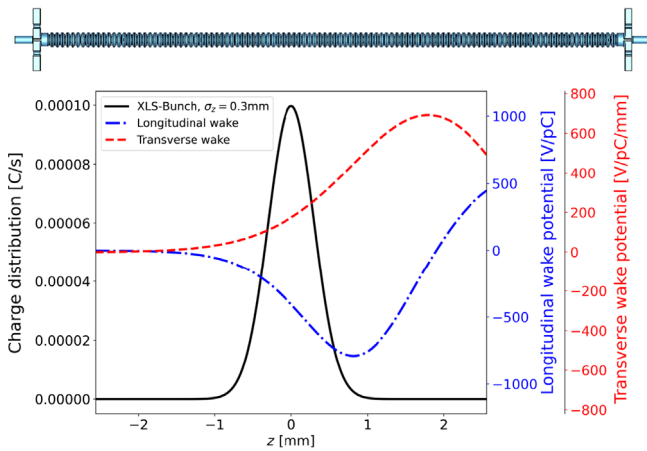


FIG. 18. Side view of the simulated 30-cm TWS (top). The magnitude of the longitudinal (dash-dotted blue line) and transverse (dashed red line) short-range wakefields (bottom), for a single 300 μm , 75 pC electron bunch.

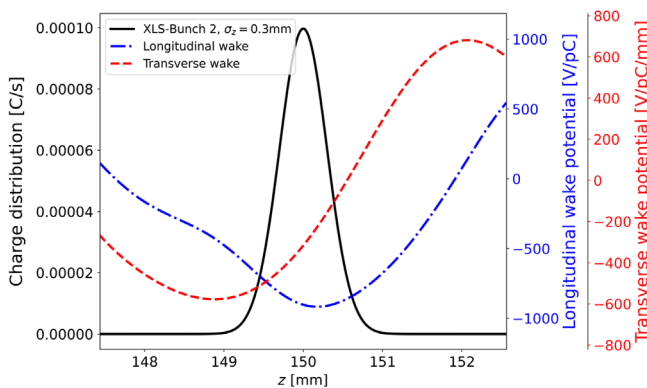


FIG. 19. Magnitude of the longitudinal (dash-dotted blue line) and transverse (dashed red line) long-range wakefields on a 30-cm TWS, as seen by a second bunch.

Any further bunch trains are considered to be too far and we neglect the wakefield contribution from the first two-bunch train.

V. KA-BAND STANDING WAVE STRUCTURES

An alternative design for the CompactLight linearizer is to use a standing wave structure (SWS). An aperture of 2 mm has been fixed, as this is the lowest aperture allowed by the wakefield studies. The general parameters of the proposed SWS cell geometry are presented in Table VI, based on Fig. 3. The maximum number of cells is limited by the cell-to-cell coupling, and hence, we set the maximum number of cells to 19.

Using an SWS would initially appear to be more efficient, as there is no power flowing out of the structure. However, there are two issues with it. The first issue is that there are no Ka-band 3-MW circulators. Therefore, the structures would need to be split and fed through hybrid

TABLE VI. SWS single cell parameters.

Parameter	Value	Units
Frequency f	36	GHz
Q factor	5941	...
Shunt impedance r_L	97.7	M Ω /m
Peak surface E field E_p^a	2.67	MV/m
Filling time T_{fill}^b	121	ns
Cavity radius R	3.86	mm
Iris radius a	2.00	mm
Cell length L_c	4.16	mm
Iris thickness L_i	0.667	mm
Cavity blending radius r_b	1.00	mm

^aNormalized to $E_{\text{acc}} = 1$ MV/m

^bTime to fill 99% of the steady-state electrical field

couplers to cancel out the reflections in pairs, by choosing the correct phase delay between each structure. Several structures are also required, as there is a limit to the number of cells that can be used in an SWS, and also the Ka-band cells are very short. The second issue is that the longer filling time of the structure leads to significantly longer SLEDII pulse compressor delay lines. A fully filled standing wave structure, which requires a pulse length of between 120 and 150 ns, would require a delay line that is more than 8.5 m long. This second issue can be avoided by partly filling the structure, as the difference between the maximum voltage and the instantaneous voltage in a standing wave structure decreases exponentially. Thus, an SWS fills very quickly at the start of the pulse. For example, if a 50-ns rectangular pulse is used in this structure, it will fill up to 85% of the maximum voltage.

A standing wave structure option is retained as an alternative due to its lower average power requirement. The TWS requires around 15 MW of input power, which needs a 0.5 μs pulse from the multibeam klystron/gyro-klystron, resulting in an average power dissipated per unit length along the structure of 2.47 kW/m at a 1-kHz repetition frequency, which is comparable to the main linac. As stated earlier, structure heating suggests that the maximum allowable heat load per unit length, based on the temperature gradient across the iris, is independent of the cavity frequency if the geometry is scaled proportionally. In the event that the smaller Ka-band structures cannot handle the same power per unit length as the main linac, then we would require an option with a lower heat load.

The SWS design is based on either two or four 19-cell standing wave structures.

If we investigate the dissipated power per unit length, as shown in Fig. 20, we find it depends weakly on the pulse length for a given accelerating voltage, but it is strongly dependent on the number of structures. We chose to look at multiples of 2, due to the requirement to cancel reflections using a hybrid coupler, as circulators are not available at this frequency and power. We then find that the minimum number of structures required is four. A pulse length of

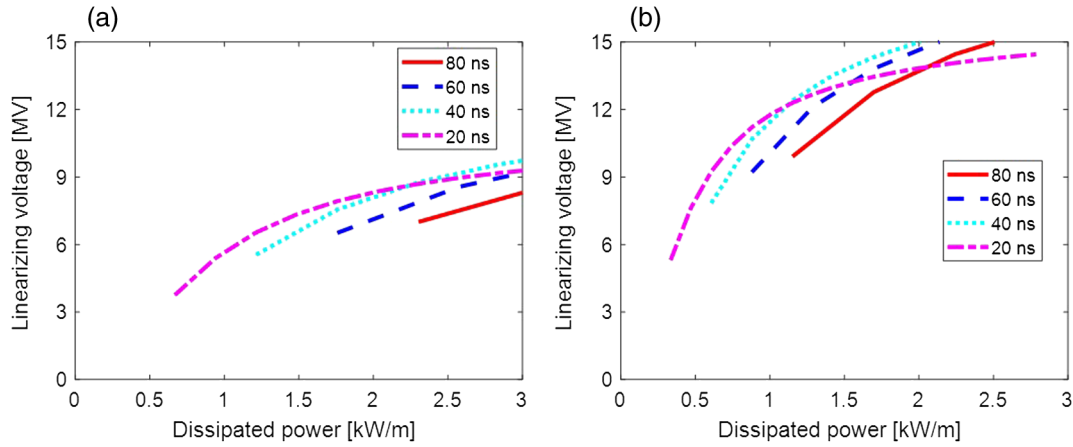


FIG. 20. Linearizing voltage as a function of dissipated power per unit length and pulse length for (a) Two SWS; (b) Four SWS.

21 ns is chosen to meet the required voltage with four structures with low dissipated power while keeping the length of the SLEDII delay line manageable. Each structure would require a peak input power of 2.84 MW, to achieve a total integrated voltage of 12.75 MV, meaning that if we keep a similar delay line length than that of the design described in Sec. III, based on Fig. 9, we would only need a 156-ns pulse from the amplifier. The gradient of the structure is 40.34 MV/m. A length of 1.50 m is chosen for the dual-moded SLEDII pulse compressor delay line to increase the input power to the standing wave structures. This length is similar to the one needed for the TWS option and will give us an output pulse width of 21 ns, which includes the rise and fall edges of the rf power source. The SWS could be partially filled to 68% of the steady-state voltage with the whole compressed pulse. This results in a lower power dissipation per unit length of 1.2 kW/m. However, three hybrid couplers are needed to cancel out the reflection, which makes the whole system complicated, and is for this reason that we leave this option as a backup alternative, in case the power handling capabilities of the TWS present a system limitation.

VI. OTHER OPTIONS

If we were to tolerate higher wakefields, then, a smaller aperture design that operates at significantly higher gradients could also be considered. An ultracompact Ka-band SWS linearizer, 8 cm long, working on π mode, with an ultrahigh accelerating gradient (beyond 100 MV/m) has been developed by INFN [24–27]. This design uses a 1-mm aperture and reaches up to 125 MV/m. In order to achieve an integrated voltage of at least 15 MV, two separated normal conducting SWS, coupled via an rf hybrid coupler, to avoid reflections returning to the rf source, are required. The average rf power per meter is almost twice that of the lower gradient structure.

A cryogenically cooled version of this structure has also been proposed for the compact XLS project at UCLA [28].

The advantages of cryogenic structures at high frequency are reduced but still provide an improvement over room temperature structures. Assuming an input power of 8 MW, it is possible to achieve an integrated voltage of about 15 MV with a single cryogenic structure, although this would need to be split into two structures, fed by a hybrid, to avoid reflections. However, this structure also has a smaller aperture than is considered allowable for CompactLight, and for this reason, it is not considered as the first option. Nevertheless, it is worth noting that for a different project, where the aperture limitations are not so stringent, this could be an interesting option to explore.

VII. CONCLUSION

In this paper, we have demonstrated that a Ka-band system with a sufficient aperture is not only capable of producing the required voltage for the linearization needed on a hard x-ray light source but is also likely superior to lower frequency rf systems. The baseline rf system for the CompactLight linearizer is a 300-mm long traveling wave structure, with an aperture of 2-mm radius, based on its relative simplicity. Such a system is capable of operating at 1 kHz with an excess of 12 MV of integrated voltage and hence a gradient of around 42.5 MV/m. The partially filled standing wave solution is retained as an alternative option, due to its possibility of running with significantly lower average power loss per unit length.

The developments in this paper open up higher-frequency rf systems for use in particle accelerators. With much shorter filling times, the potential for higher gradients is greatly improved and, with further development, reachable in the near future.

ACKNOWLEDGMENTS

CompactLight is a design study that has received funding from the European Union’s Horizon2020 research and innovation program under Grant Agreement No. 777431.

- [1] S. Di Mitri *et al.*, *Photonics* **7**, 125 (2020).
- [2] W. Wuensch, CLIC 30 GHz accelerating structure development, CERN, Geneva, Technical Report No. CERN-PS-2002-059-RF, 2002.
- [3] H. H. Braun, S. Döbert, L. Groening, I. H. Wilson, and W. Wuensch, Status of CLIC high-gradient studies, CERN, Geneva, Technical Report No. CLIC Note 532, 2001.
- [4] W. Wuensch, C. Achard, H. H. Braun, G. Carron, R. Corsini, A. Grudiev, S. T. Heikkinen, D. Schulte, J. P. H. Sladen, I. V. Syratchev, F. A. Tecker, and I. H. Wilson, 30 GHz power production in CTF3, CERN, Geneva, Technical Report No. CERN-AB-2005-030, 2005.
- [5] I. V. Syratchev, Efficient rf power extraction from the CLIC power extraction and transfer structure (PETS), Technical Report No. CERN-OPEN-2003-017, CLIC-Note-571, 2003.
- [6] CLIC and C. Collaborations, The Compact Linear Collider (CLIC)—2018 Summary Report, CERN, Geneva, CERN Yellow Reports: Monographs, 2018.
- [7] N. Zaitsev, Y. Guznov, S. Kuzikov, M. Plotkin, E. Tai, and A. Shevchenko, *Radiophys. Quantum Electron.* **56**, 492 (2014).
- [8] K. Bane, Report No. SLAC-PUB-9663, 2003.
- [9] A. Latina, The 1D tracking code, Track1D, 2020.
- [10] L. Wang, W. H. Kun Dong, Y. L. Jianxun Wang, K. R. Adrian W. Cross, and A. D. R. Phelps, *IET Microwave Antennas Propag.* **12**, 1752 (2018).
- [11] L. J. R. Nix, L. Zhang, W. He, C. R. Donaldson, K. Ronald, A. W. Cross, and C. G. Whyte, *Phys. Plasmas* **27**, 053101 (2020).
- [12] J. C. Cai, I. Syratchev, and G. Burt, *IEEE Trans. Electron Devices* **67**, 5736 (2020).
- [13] D. Farkas, H. Hogg, G. Loew, and P. Wilson, in *Proceedings of 9th International Conference on High Energy Accelerators, Stanford, CA, 1974* (A.E.C., Washington, DC, 1974).
- [14] P. Wang, H. Zha, I. Syratchev, J. Shi, and H. Chen, *Phys. Rev. Accel. Beams* **20**, 112001 (2017).
- [15] J. W. Wang, S. G. Tantawi, C. Xu, M. Franzi, P. Krejcik, G. Bowden, S. Condamoor, Y. Ding, V. Dolgashev, J. Eichner, A. Haase, J. R. Lewandowski, and L. Xiao, *Phys. Rev. Accel. Beams* **20**, 110401 (2017).
- [16] P. Wilson, Z. Farkas, and R. Ruth, in *Proceedings of the Linear Accelerator Conference, Albuquerque, NM, 1990* (Los Alamos National Laboratory, Albuquerque, NM, 1990).
- [17] S. G. Tantawi, R. J. Loewen, C. D. Nantista, and A. E. Vliet, *IEEE Trans. Microwave Theory Tech.* **47**, 2539 (1999).
- [18] S. V. Kuzikov, A. A. Vikharev, M. E. Plotkin, D. Y. Shegol'kov, and J. L. Hirshfield, *Phys. Rev. ST Accel. Beams* **10**, 082001 (2007).
- [19] J. Sauza-Bedolla, S. Atieh, and N. C. Lasheras, in *Proceedings of 29th Linear Accelerator Conference (LINAC'18), Beijing, China, 2018* (JACoW, Geneva, Switzerland, 2019), pp. 374–376.
- [20] T. Higo, K. Kubo, and K. Yokoya, in *Proceedings of the 18th Particle Accelerator Conference, New York, 1999* (IEEE, New York, 1999), Vol. 5, pp. 3435–3437.
- [21] K. N. Sjobak, E. Adli, and A. Grudiev, New criterion for shape optimization of normal-conducting accelerator cells for high-gradient applications, CERN, Geneva, Technical Report No. CERN-ACC-2014-408, 2014.
- [22] A. Grudiev, S. Calatroni, and W. Wuensch, *Phys. Rev. ST Accel. Beams* **12**, 102001 (2009).
- [23] D. P. Pritzkau, RF pulsed heating, Stanford Linear Accelerator Center, Menlo Park, CA, Technical Report No. SLAC-R-577, 2002.
- [24] B. Spataro and M. Behtouei, in On behalf of the SPARC—LAB collaboration, Compact Light XLS project, WP3 Status Reports, Workshop in Trieste, Italy, <https://indico.cern.ch/event/733115> (2018).
- [25] B. Spataro, A possible linearizer at 35.982 GHz, in *Proceedings of the First Annual Meeting of the Compact Light XLS Project, Barcelona, Italy, 2018* (2018), 10.13140/RG.2.2.27217.68968.
- [26] M. Behtouei, L. Faillace, M. Ferrario, B. Spataro, and A. Variola, *J. Phys. Conf. Ser.* **1596**, 012021 (2020).
- [27] M. Behtouei, L. Faillace, B. Spataro, A. Variola, and M. Migliorati, *Nucl. Instrum. Methods Phys. Res., Sect. A* **984**, 164653 (2020).
- [28] B. Spataro, M. Behtouei, L. Faillace, A. Variola, V. Dolgashev, J. Rosenzweig, G. Torrisi, and M. Migliorati, *Nucl. Instrum. Methods Phys. Res., Sect. A* **1013**, 165643 (2021).